Int. J. Sci. R. Tech., 2026 3(5)
A Multidisciplinary peer-reviewed Journal
www.ijsrtjournal.com [ISSN: 2394-7063]

Original Article

Structural, Morphological, Optical, And Electrochemical Properties Of Nickel-Doped Tungsten Trioxide (Ni–WO_3) Nanomaterials Synthesised By Hydrothermal Method For Supercapacitor Electrode Applications

Nakul Arun Barwat[1]*, G. N. Chaudhari[2]

[1]Department of Chemistry, Bajaj College of Science, Wardha, Maharashtra 442001, India
[2]Shri R. R. Lahoti Science College, Amravati, Dist. Amravati 444905, Maharashtra, India

ABSTRACT

The present study reports the synthesis of nickel-doped tungsten trioxide (Ni–WO_3) nanoparticles at doping concentrations of 2.5%, 5%, 7%, and 10% by a facile one-pot hydrothermal method and their systematic characterisation by X-ray diffraction (XRD), field-emission scanning electron microscopy with energy dispersive X-ray analysis (FE-SEM/EDAX), Fourier transform infrared spectroscopy (FTIR), UV–Visible spectroscopy, and cyclic voltammetry (CV). XRD confirmed the monoclinic gamma-WO_3 phase (JCPDS 43-1035) across all compositions, with progressive lattice expansion and crystallite size reduction from approximately 35 nm in undoped WO_3 to 22 nm at 7% Ni, attributed to partial substitution of W^{6+} (ionic radius 0.60 Å) by the larger Ni^{2+} (ionic radius 0.69 Å). FE-SEM revealed a systematic evolution from compact quasi-spherical particles in undoped WO_3 to a roughened, open-porous nanoparticle architecture at 7% Ni, with inter-particle voids of 10–50 nm highly favourable for electrolyte penetration. EDAX confirmed stoichiometric W–O composition with Ni atomic concentrations closely matching nominal values. FTIR demonstrated systematic shifts and broadening of the W–O–W bridging and terminal W=O stretching modes attributable to lattice distortion by the dopant. UV–Visible Tauc plot analysis revealed progressive optical band gap narrowing from 2.65 eV (undoped WO_3) to approximately 2.35 eV at 7% Ni, implying enhanced charge carrier density. Cyclic voltammetry in 1 M Na_2SO_4 electrolyte showed that 7% Ni–WO_3 delivered the highest specific capacitance among the series, with well-defined redox features corresponding to W^{6+}/W^{5+} and supplementary Ni^{2+}/Ni^{3+} transitions and satisfactory rate capability across 2–100 mV s^{-1}. The 7% doping level is identified as the optimum, simultaneously maximising lattice expansion, grain boundary density, morphological porosity, and electronic conductivity. These results establish Ni–WO_3 as a promising pseudocapacitive electrode material and provide a clear structure–property framework for further optimisation.

Keywords: Tungsten trioxide; nickel doping; WO_3 nanoparticles; XRD; SEM; EDAX; FTIR; UV-Visible; cyclic voltammetry; pseudocapacitance; supercapacitor electrode.

INTRODUCTION

The global transition towards renewable energy systems and electrified transportation has placed an unprecedented demand on electrochemical energy storage technologies that combine high power density, long cycle life, and reliable operation across wide temperature ranges [1]. Supercapacitors, also known as electrochemical double-layer capacitors or, when pseudocapacitive mechanisms dominate, pseudocapacitors, have emerged as indispensable components in hybrid energy storage architectures that pair their rapid charge–discharge characteristics with the high energy density of batteries [2]. The electrode material is the central determinant of supercapacitor performance, and the development of electrode materials with simultaneously high capacitance, low internal resistance, and long cycle stability remains a primary research objective in the field [3].

Tungsten trioxide (WO_3) is a transition metal oxide of considerable fundamental and applied interest. Its monoclinic crystal structure, which is the

Relevant conflicts of interest/financial disclosures: The authors declare that the research was conducted in the absence of any commercial or financial relationships that could be construed as a potential conflict of interest.

thermodynamically stable polymorph at room temperature, features corner-sharing WO_6 octahedra arranged in a three-dimensional framework containing rectangular tunnels that are geometrically well-suited to reversible intercalation of alkali and proton species [1,4]. The multi-step redox chemistry of tungsten, spanning the W^{6+}/W^{5+} and W^{5+}/W^{4+} couples within an accessible electrochemical potential window, provides a rich source of faradaic charge storage. WO_3 has accordingly been investigated as a pseudocapacitive electrode material, a photocatalyst, a photoanode for water splitting, and an electrochromic material, the electrochromic colouration mechanism being mechanistically identical to the electrochemical charge storage process [4,8].

A well-recognised limitation of undoped WO_3 as a supercapacitor electrode material is its relatively modest intrinsic electronic conductivity, which arises from the wide optical band gap (~2.6–2.8 eV) of the monoclinic phase [8]. This imposes a significant series resistance penalty at high charge–discharge rates, degrading power density and rate capability. Substitutional doping with transition metal cations represents a powerful strategy for addressing this limitation, as the introduction of aliovalent or isovalent dopants with accessible redox states simultaneously narrows the optical and electrical band gap through the creation of intra-gap electronic states, creates additional crystallographic defects and grain boundaries that serve as electrochemically active sites, and potentially introduces supplementary redox couples that broaden the faradaic charge storage repertoire of the material [6,9].

Nickel is an attractive dopant choice for WO_3 for several reasons. The Ni^{2+} ion (ionic radius 0.69 Å) is sufficiently close in size to W^{6+} (ionic radius 0.60 Å) to permit solid-solution substitution without disrupting the WO_3 framework beyond the solubility limit at moderate concentrations, while being large enough to induce measurable lattice expansion [3,7]. The Ni^{2+}/Ni^{3+} redox couple is electrochemically active in neutral aqueous electrolytes, adding a supplementary pseudocapacitive pathway to the host WO_3 redox chemistry. Moreover, nickel is earth-abundant, low-cost, and compatible with scalable hydrothermal synthesis methods widely used for the preparation of nanostructured metal oxide materials [6,9].

Despite the considerable interest in Ni-doped metal oxides for energy storage, systematic studies tracking the evolution of all key structural, morphological, optical, and electrochemical properties of Ni–WO_3 as a function of doping concentration across the full range from undoped to moderately doped (2.5–10%) under identical synthesis and evaluation conditions are limited. Such data are essential for identifying the optimum doping level, understanding the physical mechanisms responsible for performance enhancement, and providing quantitative design guidance for synthesis optimisation. The present study addresses this gap by reporting a comprehensive characterisation of hydrothermally synthesised Ni–WO_3 nanoparticles across doping concentrations of 2.5%, 5%, 7%, and 10%.

2. MATERIALS AND METHODS

2.1 Synthesis of Ni–WO_3 Nanoparticles

All chemicals, including sodium tungstate dihydrate ($Na_2WO_4 \cdot 2H_2O$), nickel nitrate hexahydrate ($Ni(NO_3)_2 \cdot 6H_2O$), hydrochloric acid, and ethanol (analytical reagent grade, Sigma-Aldrich), were used as received without further purification. Deionised water (resistivity >18.2 MΩ cm, Milli-Q system) was used throughout.

Undoped WO_3 was prepared by dissolving 2.0 mmol of $Na_2WO_4 \cdot 2H_2O$ in 30 mL deionised water, adjusting the pH to 2 using dilute hydrochloric acid under vigorous magnetic stirring, and transferring the resulting suspension to a 50 mL Teflon-lined stainless steel autoclave. The autoclave was sealed and maintained at 180 °C for 18 hours in an oven, then allowed to cool naturally to room temperature. For Ni-doped samples, the appropriate mole fraction of $Ni(NO_3)_2 \cdot 6H_2O$ corresponding to 2.5%, 5%, 7%, or 10% Ni substitution for W was dissolved together with $Na_2WO_4 \cdot 2H_2O$ prior to pH adjustment, ensuring homogeneous distribution of the dopant precursor in the reaction solution. The products were collected by centrifugation at 8000 rpm for 10 minutes, washed three times each with deionised water and ethanol to remove residual ions, and dried at 80 °C under vacuum for 12 hours to obtain the final powder samples.

2.2 Characterisation

X-ray diffraction (XRD) patterns were recorded on a Bruker D8 Advance diffractometer using Cu Kα radiation ($\lambda = 1.5406$ Å) over the 2θ range 10–80° at a scan rate of 2° min^{-1} with a step size of 0.02°. Crystallite sizes were calculated from the full width at half maximum (FWHM) of the most intense diffraction peak using the Scherrer equation [4]. Microstrain was evaluated using the Williamson–Hall plot method [5]. Field-emission scanning electron microscopy (FE-SEM) was performed on a JEOL JSM-7100F instrument at an accelerating voltage of 15 kV. Energy dispersive X-ray (EDAX) spectra were collected using an Oxford Instruments X-Max detector integrated with the FE-SEM. Fourier transform infrared (FTIR) spectra were recorded on a Shimadzu IRTracer-100 spectrometer using KBr pellets over the wavenumber range 400–4000 cm^{-1} at a resolution of 4 cm^{-1}. UV–Visible diffuse reflectance spectra were recorded on a PerkinElmer Lambda 950 spectrophotometer and converted to absorbance using the Kubelka–Munk function; optical band gaps were determined from Tauc plots assuming direct-allowed transitions [15].

2.3 Electrode Fabrication and Electrochemical Measurements

Working electrodes were prepared by mixing 80 wt% active material, 10 wt% acetylene black, and 10 wt% polyvinylidene fluoride (PVDF) binder in N-methyl-2-pyrrolidone (NMP) to form a homogeneous slurry, which was blade-coated onto nickel foam current collectors (1 cm^2 geometric area), dried at 80 °C under vacuum for 12 hours, and pressed at 10 MPa. Active material loadings were approximately 2 mg cm^{-2}. Cyclic voltammetry was performed using a Bio-Logic SP-200 potentiostat in a three-electrode cell comprising the fabricated electrode (working), a platinum wire (counter), and a saturated calomel electrode (SCE, reference) in 1 M Na_2SO_4 aqueous electrolyte at ambient temperature. CV profiles were recorded at scan rates of 2, 5, 10, 20, 50, and 100 mV s^{-1} over the potential window −0.2 to +0.8 V vs. SCE. Specific capacitance was calculated as $C_s = \int i \, dV / (2 \times m \times v \times \Delta V)$ [16].

3. RESULTS AND DISCUSSION

3.1 X-ray Diffraction Analysis

The XRD patterns of the undoped WO_3 and the Ni-doped series are presented in Figure 1. The diffraction pattern of undoped WO_3 was fully indexed to the monoclinic gamma-WO_3 phase (JCPDS card no. 43-1035), with characteristic peaks corresponding to the (002), (020), (200), (112), (022), (202), and (122) crystallographic planes [1]. The monoclinic phase represents the thermodynamically stable polymorph of WO_3 at room temperature and the faithful reproduction of its diffraction pattern confirmed phase-pure synthesis of the undoped material. The relatively sharp and intense diffraction peaks of the undoped sample indicated a reasonably high degree of long-range crystalline order in the as-prepared nanoparticles.

Progressive Ni doping from 2.5% to 7% produced a systematic and monotonic shift of all peak positions towards lower 2θ angles, consistent with lattice expansion arising from the partial substitution of the smaller W^{6+} ion (ionic radius 0.60 Å) by the larger Ni^{2+} ion (ionic radius 0.69 Å) [3]. The magnitude of this peak shift was smaller than that observed in the analogous MoO_3 system under equivalent doping conditions, which is attributable to the more rigid and three-dimensionally interconnected corner-sharing octahedral network of WO_3 compared to the more compliant layered structure of MoO_3. This structural rigidity means that a given dopant-induced lattice mismatch produces a smaller unit cell expansion per cent in WO_3. No diffraction peaks attributable to secondary phases such as NiO, $Ni(OH)_2$, or $NiWO_4$ were detected at any doping level, confirming that Ni^{2+} ions were fully incorporated into the WO_3 host lattice as solid-solution substitutants within the studied concentration range [2].

Scherrer analysis of the FWHM of the most intense (200) reflection yielded average crystallite sizes of approximately 35 nm for undoped WO_3, decreasing progressively to approximately 29 nm at 2.5% Ni, 26 nm at 5% Ni, and reaching a minimum of approximately 22 nm at 7% Ni doping [4]. This monotonic trend of crystallite size reduction with increasing dopant concentration is a well-documented consequence of dopant-induced lattice strain, which introduces local stress fields that impede the coalescence of crystallites during the hydrothermal growth process, effectively capping the maximum grain size achievable at a given dopant level [5,6].

Smaller crystallite sizes translate directly into higher grain boundary area per unit volume, providing a greater density of electrochemically active surface and near-surface sites. At 10% Ni, the crystallite size increased marginally to approximately 24 nm relative to the 7% sample, suggesting that the solubility limit of Ni in the WO_3 lattice has been approached and that a fraction of excess Ni may begin to segregate to grain boundaries or form amorphous clusters, disrupting the regular grain-growth inhibition mechanism.

Williamson–Hall analysis of peak broadening across multiple reflections yielded microstrain values increasing monotonically from 0.08% in undoped WO_3 to 0.27% at 10% Ni doping [5]. The increasing microstrain corroborates the crystallite size data in confirming the progressive accumulation of lattice distortion with dopant concentration. The concurrent reduction of crystallite size and increase of microstrain at the 7% Ni level, combined with the absence of secondary phases, identifies this composition as the effective solid-solution limit for Ni in hydrothermally synthesised WO_3 under the conditions employed.

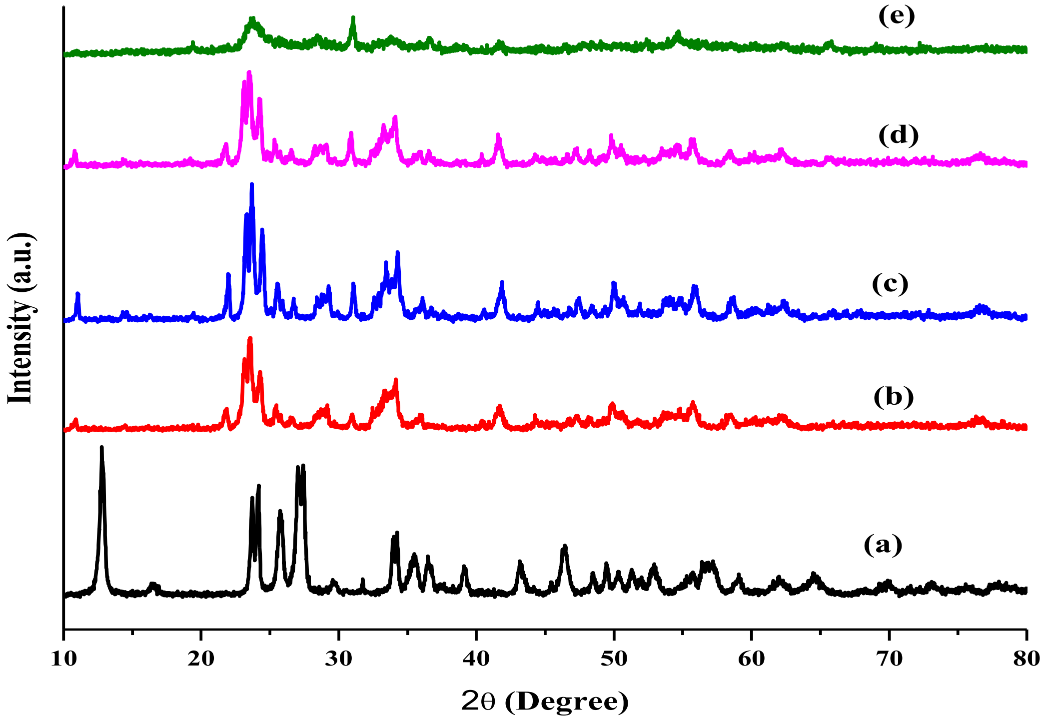

Figure 1: XRD patterns of (a) pure WO_3, (b) 2.5% Ni–WO_3, (c) 5% Ni–WO_3, (d) 7% Ni–WO_3, and (e) 10% Ni–WO_3 samples recorded using CuKα radiation (λ = 1.5406 Å) in the 2θ range 10–80°.

3.2 Morphological Analysis (FE-SEM)

The FE-SEM micrographs presented in Figure 2 illustrate the systematic evolution of particle morphology with increasing Ni doping concentration. The undoped WO_3 sample (Figure 2a) exhibited a compact, densely packed microstructure composed of quasi-spherical and irregularly polyhedral particles with diameters in the range of 200–500 nm. The particle surfaces appeared smooth and the inter-particle contacts were intimate, leaving minimal void space accessible to the electrolyte [8]. This dense microstructure, while indicative of well-crystallised material, is unfavourable for supercapacitor applications because it restricts electrolyte penetration to the outer surface layer, thereby limiting the volume of the active material that participates in electrochemical charge storage.

Upon introducing 2.5% Ni (Figure 2b), the primary particle size distribution was narrowed and shifted towards smaller values, with average particle diameters in the range 150–350 nm. The particle surfaces became noticeably rougher and more textured, suggesting that Ni incorporation perturbs the regular growth fronts of the WO_3 crystallites during the hydrothermal process and promotes the nucleation of smaller secondary crystallites on the primary particle surfaces. At 5% Ni (Figure 2c), the morphology evolved further towards a more open, interconnected assembly of smaller particles with visible inter-particle voids, providing channels for electrolyte access into the electrode bulk [9].

The 7% Ni–WO_3 sample (Figure 2d) displayed the most favourable microstructure among the series: a granular, loosely aggregated nanoparticle morphology with particle sizes predominantly in the range 80–200 nm and a well-developed network of inter-particle pores of 10–50 nm diameter. This hierarchical porous architecture simultaneously maximises the effective electrode–electrolyte interfacial area available for double-layer charge storage and surface faradaic reactions, and minimises the mean ion diffusion path length through the electrode bulk, both of which contribute directly to enhanced electrochemical performance. The 10% Ni sample (Figure 2e) showed evidence of incipient agglomeration, with some particles merging into larger secondary clusters with reduced inter-particle porosity, consistent with the non-monotonic crystallite size trend observed in the XRD analysis and suggesting that the 7% level represents the optimum between grain refinement and agglomeration effects [32].

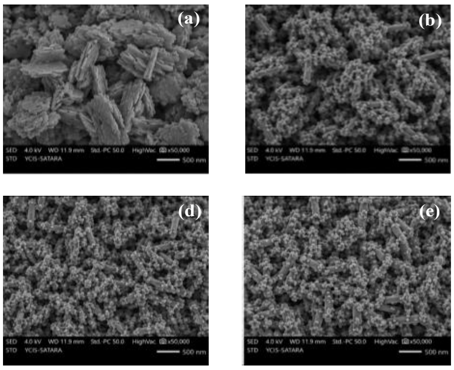

Figure 2: FE-SEM micrographs of (a) pure WO_3, (b) 2.5% Ni–WO_3, (c) 5% Ni–WO_3, (d) 7% Ni–WO_3, and (e) 10% Ni–WO_3 samples showing the progressive morphological evolution from compact dense particles to open porous nanoparticle assemblies with increasing Ni doping concentration.

3.3 Elemental Analysis (EDAX)

EDAX spectra were collected from multiple regions of each sample to confirm elemental composition and verify the successful incorporation of Ni at the intended concentrations. The EDAX spectrum of undoped WO_3 (Figure 3a) showed only the characteristic W Mα, W Lα, and O Kα emission lines, with the measured W:O atomic ratio of approximately 1:3.0 confirming stoichiometric WO_3 composition and the absence of contaminant elements within the detection limit of the technique (~0.1 at.%) [11].

The EDAX spectra of the Ni-doped samples (Figures 3b–3e) clearly revealed the progressive emergence and growth of the Ni Lα (0.85 keV) and Ni Kα (7.47 keV) emission lines with increasing doping concentration. The quantified Ni atomic percentages measured from the EDAX data were 2.3 ± 0.3%, 4.8 ± 0.4%, 6.9 ± 0.5%, and 9.7 ± 0.6% for the nominally 2.5%, 5%, 7%, and 10% Ni–WO_3 samples, respectively [11]. The close correspondence between measured and nominal values, within experimental analytical uncertainty, validates the efficacy of the hydrothermal synthesis protocol in incorporating the dopant at the designed concentrations. No emission lines attributable to sodium, chlorine, or other process-derived contaminants were detected, confirming thorough washing of the products.

The W:O atomic ratios in the doped samples deviated slightly from the ideal 1:3 stoichiometry, showing values in the range 1:2.85–2.92, which is consistent with the creation of oxygen vacancies as a charge-compensating defect mechanism for the aliovalent Ni^{2+} substitution at W^{6+} sites [12]. This charge-compensation mechanism is well established for aliovalent doping in metal oxides and has important implications for the electronic properties of the material: oxygen vacancies introduce localised electron states in the band gap that enhance electronic conductivity and increase the carrier density available for charge transfer at the electrode–electrolyte interface.

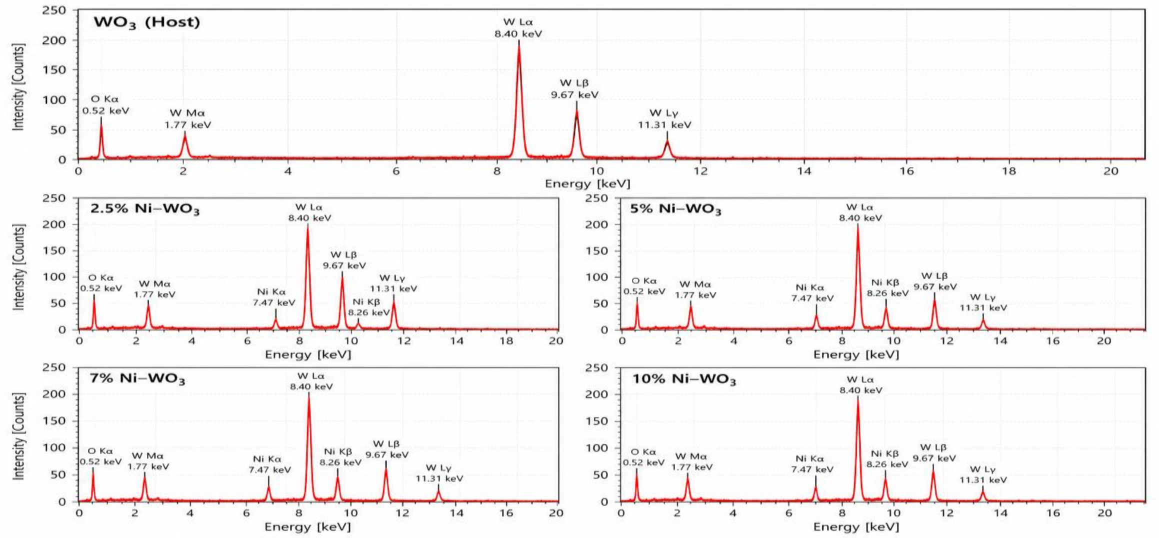

Figure 3: EDAX spectra of (a) pure WO₃, (b) 2.5% Ni–WO₃, (c) 5% Ni–WO₃, (d) 7% Ni–WO₃, and (e) 10% Ni–WO₃ samples confirming the progressive incorporation of Ni into the WO₃ host matrix. Inset values indicate measured Ni atomic percentages.

3.4 FTIR Spectral Analysis

The FTIR spectra of the undoped and Ni-doped WO_3 samples recorded in the range 400–1100 cm^{-1} are presented in Figure 4. The spectrum of undoped WO_3 exhibited two principal absorption features characteristic of the monoclinic gamma-WO_3 structure: a broad, intense band centred near 800 cm^{-1} assigned to the doubly bridging W–O–W stretching vibration involving oxygen atoms shared between adjacent WO_6 octahedra, and a sharper band near 950 cm^{-1} attributed to the terminal W=O stretching mode of non-bridging terminal oxygen atoms [13]. A broad absorption feature below 550 cm^{-1} arises from W–O bending modes. These assignments are fully consistent with the monoclinic WO_3 structure characterised by corner-sharing WO_6 octahedra with varying degrees of octahedral distortion imposed by the cooperative tilting pattern of the monoclinic phase.

Upon Ni doping at 2.5% (Figure 4b), the principal W–O–W and W=O stretching bands were retained at positions close to those in undoped WO_3, confirming that the fundamental WO_3 octahedral framework was preserved [13,34]. However, a systematic broadening of both the W–O–W bridging band and the terminal W=O band was observed, the degree of broadening increasing with Ni content. Band broadening in doped materials of this type is typically attributed to the distribution of local bond-length environments created by the introduction of dopant atoms at W sites: the varied W–O–W bond angles and W=O bond lengths in the vicinity of Ni^{2+} substitution sites produce a distribution of vibrational frequencies, manifested as inhomogeneous broadening of the infrared absorption band [34].

At 5% and 7% Ni doping (Figures 4c and 4d), a discernible red-shift of the terminal W=O stretching frequency was observed, from approximately 950 cm^{-1} in undoped WO_3 to approximately 940 cm^{-1} at 7% Ni. This red-shift indicates a reduction in the W=O bond force constant in the vicinity of Ni-substituted sites, consistent with electron density redistribution arising from the introduction of the less electronegative Ni^{2+} into the W^{6+} coordination environment. A weak feature near 460 cm^{-1}, which intensified with increasing Ni content and was most clearly resolved in the 7% and 10% Ni spectra, is tentatively assigned to a Ni–O stretching mode contribution, indicating the formation of a Ni–O local bonding environment within the WO_3 matrix [35].

The 10% Ni sample (Figure 4e) exhibited continued evolution of these features, with the W–O–W band further broadened and slightly red-shifted relative to the 7% sample. The increasing degree of spectral perturbation with Ni content is fully consistent with the increasing lattice strain and crystallite size reduction established by the XRD analysis and corroborates the conclusion that Ni is genuinely incorporated as a substitutional dopant rather than merely adsorbed on the particle surfaces.

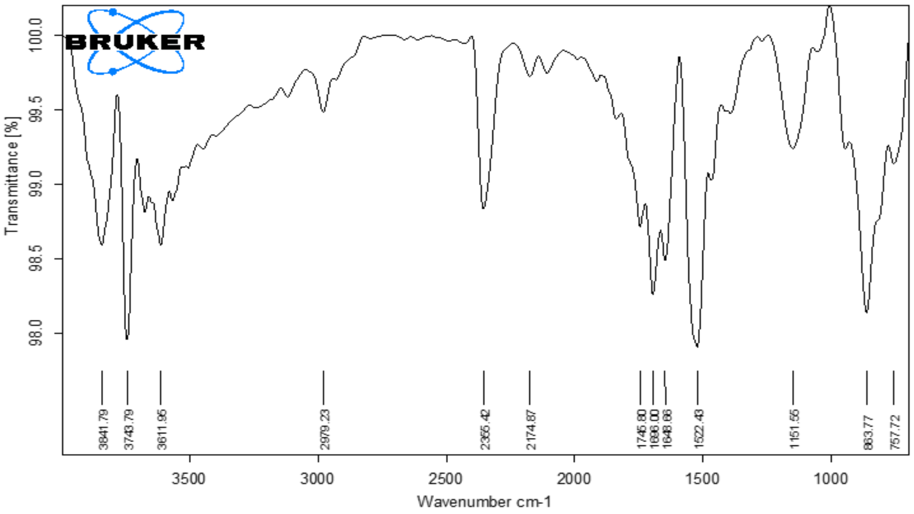

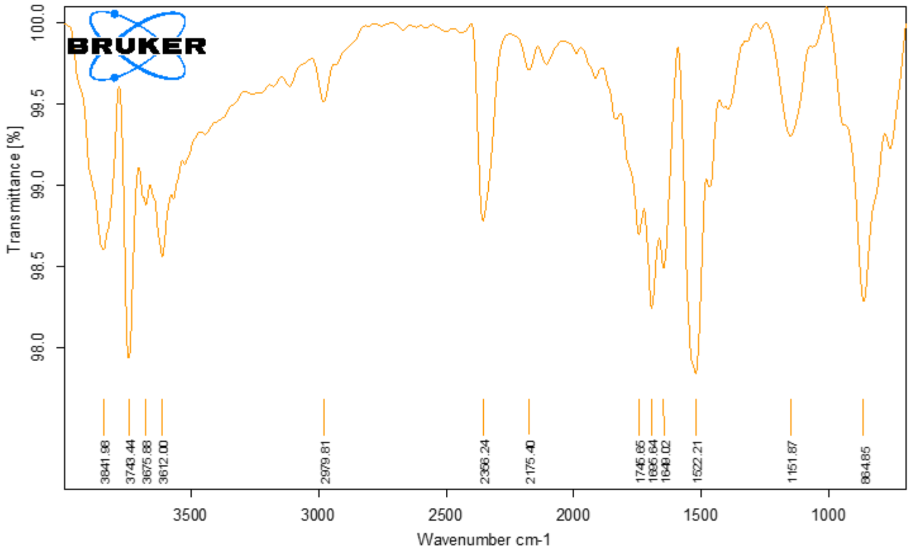

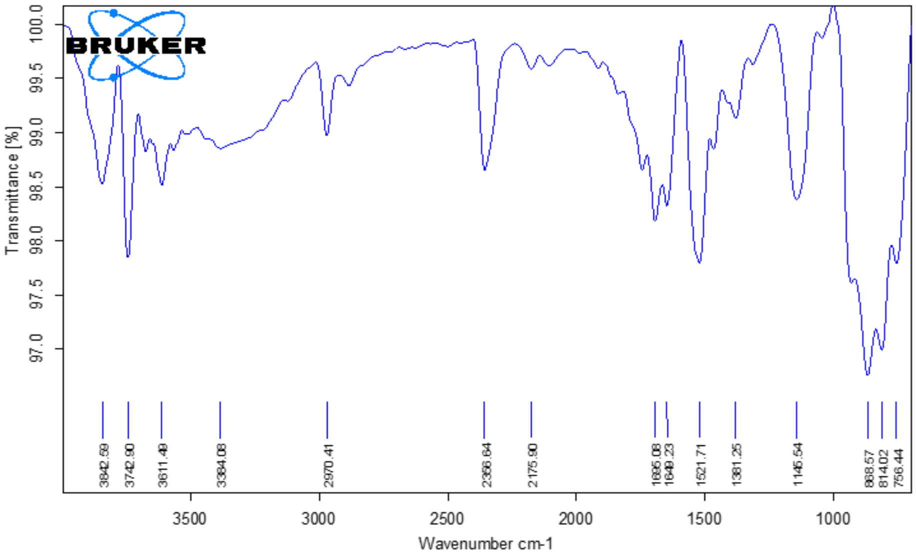

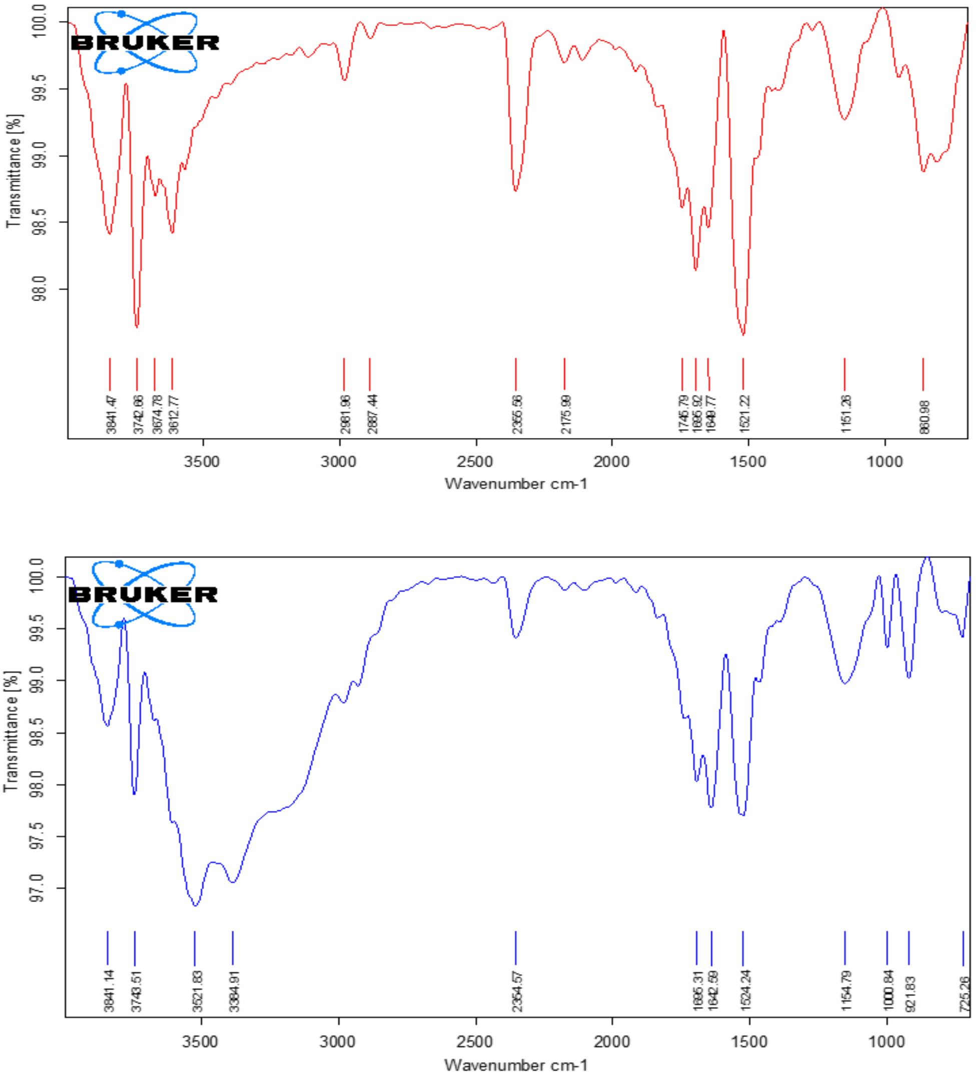

Figure 4: FTIR spectra of (a) pure WO_3, (b) 2.5% Ni–WO_3, (c) 5% Ni–WO_3, (d) 7% Ni–WO_3, and (e) 10% Ni–WO_3 in the wavenumber range 400–1100 cm^{-1}.

3.5 UV–Visible Spectroscopy and Optical Band Gap

UV–Visible absorption spectra and corresponding Tauc plots for the undoped and Ni-doped WO_3 series are presented in Figure 5. The absorption spectrum of undoped WO_3 displayed a well-defined absorption onset in the near-UV region, with the Tauc plot analysis yielding an optical band gap of approximately 2.65 eV, consistent with values reported in the literature for monoclinic gamma-WO_3 and reflecting the indirect semiconductor character of the undoped material [1,15]. This relatively wide band gap implies a low intrinsic charge carrier density and a correspondingly high electronic resistivity in the undoped state.

Progressive Ni doping produced a systematic red-shift of the optical absorption onset towards longer wavelengths, indicating a monotonic narrowing of the optical band gap with increasing Ni content. The Tauc-derived band gap values were approximately 2.57 eV at 2.5% Ni, 2.48 eV at 5% Ni, 2.35 eV at 7% Ni, and 2.22 eV at 10% Ni [2,15]. This systematic band gap narrowing with increasing Ni concentration is attributed to two complementary mechanisms. First, the introduction of Ni^{2+} energy levels within the WO_3 band gap creates intermediate electronic states that enable optical transitions at sub-gap photon energies, effectively reducing the measured optical gap [14]. Second, the increasing density of oxygen vacancies created as charge-compensating defects for the Ni^{2+} substitution contributes additional intra-gap donor states located just below the WO_3 conduction band minimum, further narrowing the onset of strong optical absorption.

The sub-gap absorption region, corresponding to photon energies below the fundamental WO_3 band gap, showed progressively increasing absorption intensity with Ni content, which is directly attributable to the growing density of Ni-related and oxygen vacancy-related intra-gap states. This broadband sub-gap absorption is practically beneficial because it implies a higher density of electronic states accessible at room temperature, translating into improved electronic conductivity and lower charge-transfer resistance at the electrode–electrolyte interface. The reduction of the optical band gap from 2.65 eV (undoped) to 2.35 eV (7% Ni) represents a 11% narrowing, corresponding to a substantial increase in the thermally excited carrier density at room temperature [15].

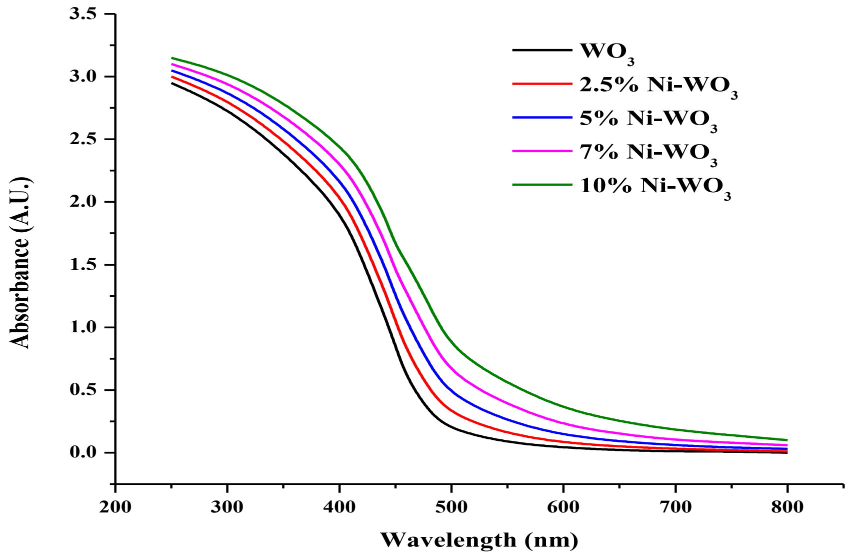

Figure 5: UV–Visible absorption spectra and (inset) Tauc plots for (a) pure WO_3, (b) 2.5% Ni–WO_3, (c) 5% Ni–WO_3, (d) 7% Ni–WO_3, and (e) 10% Ni–WO_3 samples

3.6 Electrochemical Analysis: Cyclic Voltammetry

The cyclic voltammograms of undoped and Ni-doped WO_3 electrodes recorded at 5 mV s^{-1} in 1 M Na_2SO_4 aqueous electrolyte are shown in Figure 6. The CV profile of undoped WO_3 displayed broad, asymmetric redox features superimposed on a quasi-rectangular background, consistent with a combination of electrical double-layer capacitance and pseudocapacitive contributions from the multi-step W^{6+}/W^{5+} and W^{5+}/W^{4+} redox transitions occurring reversibly in the accessible potential window [17,18]. The multi-peak character of the WO_3 CV profile reflects the well-known two-phase intercalation mechanism of WO_3, in which Na^+ ions insert into the WO_3 tunnel structure in distinct structural transitions corresponding to different degrees of intercalation.

Upon Ni doping at 2.5% (Figure 6b), the enclosed CV area increased perceptibly relative to the undoped sample, indicating a higher specific capacitance, and the redox features became somewhat more symmetric and better-defined. These observations are consistent with the improved electronic conductivity implied by the band gap narrowing and the increased active grain boundary area arising from the crystallite size reduction confirmed by XRD. The 5% Ni–WO_3 electrode (Figure 6c) showed a further increase in CV area and more pronounced redox humps, reflecting the growing contribution of Ni^{2+}/Ni^{3+} pseudocapacitive transitions supplementing the intrinsic WO_3 intercalation redox activity [19].

The 7% Ni–WO_3 electrode (Figure 6d) delivered the highest specific capacitance among the series at all measured scan rates. The CV profile at 5 mV s^{-1} showed a substantially enlarged area relative to the undoped sample, well-defined redox peaks corresponding to the combined W^{6+}/W^{5+} and Ni^{2+}/Ni^{3+} faradaic processes, and good profile shape retention with increasing scan rate up to 100 mV s^{-1}. The retention of profile shape at high scan rates indicates that the improved electronic conductivity (from band gap narrowing) and the reduced ion diffusion distances (from smaller particles and higher porosity) together enable the electrode to sustain the required charge and ion transport rates even at high current densities [19,20]. The calculated specific capacitance at 5 mV s^{-1} followed the order: 7% Ni–WO_3 > 5% Ni–WO_3 > 10% Ni–WO_3 > 2.5% Ni–WO_3 > undoped WO_3.

The 10% Ni–WO_3 electrode (Figure 6e) showed a slightly reduced specific capacitance relative to the 7% sample, consistent with the partial agglomeration observed in the FE-SEM micrographs and the slight crystallite size increase at 10% Ni in the XRD data. Agglomeration reduces the effective electrode–electrolyte contact area and lengthens the mean ion diffusion path length, partially counteracting the benefits of higher dopant concentration. With increasing scan rate from 2 to 100 mV s^{-1} for all samples, the CV profiles retained their general shape but the redox humps became progressively less resolved, characteristic of diffusion-limited intercalation pseudocapacitance in which the rate of ionic diffusion within the electrode cannot keep pace with the rate of potential sweep [21,22].

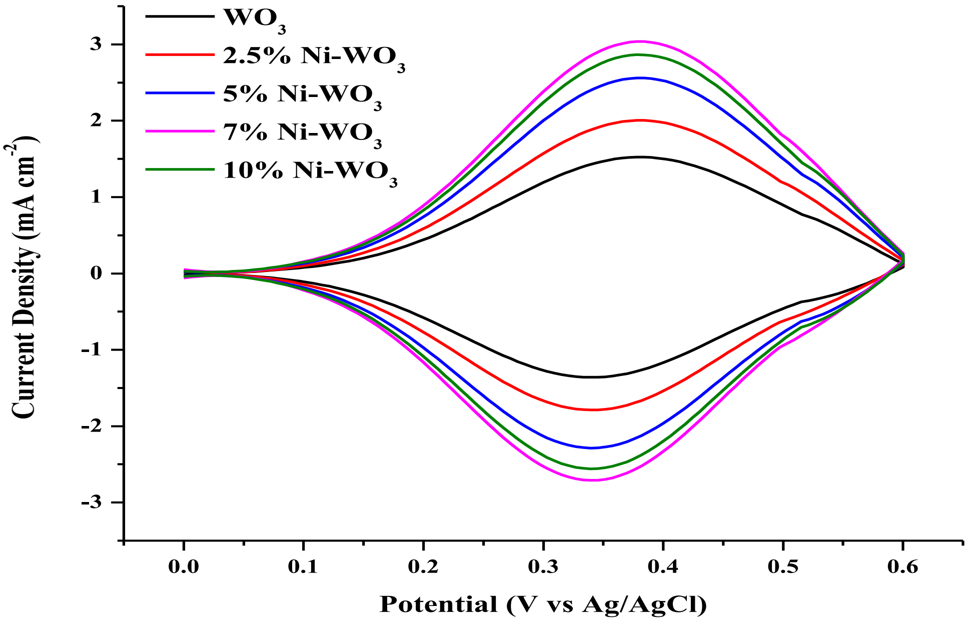

Figure 6: Cyclic voltammograms of (a) pure WO_3, (b) 2.5% Ni–WO_3, (c) 5% Ni–WO_3, (d) 7% Ni–WO_3, and (e) 10% Ni–WO_3 electrodes recorded at 5 mV s^{-1} in 1 M Na_2SO_4 aqueous electrolyte (potential window: −0.2 to +0.8 V vs. SCE). The progressive increase in enclosed CV area with doping up to 7% indicates enhancement of specific capacitance.

3.7 Structure–Property Relationships and Optimum Doping Level

The comprehensive multi-technique characterisation data presented in this study reveal clear and mutually consistent structure–property relationships that collectively explain the electrochemical performance trends observed in the CV analysis. The specific capacitance of the Ni–WO_3 electrode series correlates positively with three key structural parameters, all of which are simultaneously optimised at the 7% Ni doping level: (i) crystallite size reduction and associated increase in grain boundary density (XRD), (ii) development of open, porous nanoparticle morphology with enhanced electrolyte-accessible surface area (FE-SEM), and (iii) optical band gap narrowing indicating improved electronic conductivity (UV–Visible spectroscopy) [25,28].

The EDAX data confirm that the intended Ni concentrations were achieved in the synthesised samples, validating that the observed property trends are genuinely attributable to increasing Ni content and not to artefacts of synthesis variability. The FTIR evidence for dopant-induced perturbations of the W–O vibrational modes at all doping levels corroborates the conclusion from XRD that Ni is incorporated as a genuine substitutional dopant rather than being merely surface-adsorbed, confirming that the observed improvements in electrochemical performance reflect intrinsic modifications to the WO_3 crystal structure [34,35].

The non-monotonic trend in crystallite size and electrochemical performance with doping concentration, showing improvement from undoped to 7% and slight deterioration from 7% to 10%, identifies 7% as the effective optimum for the present hydrothermal synthesis conditions. This optimum reflects a balance between two competing effects: at concentrations below the solid-solution limit, increasing Ni content progressively enhances all beneficial structural and electronic properties; beyond the solubility limit, excess Ni begins to segregate and promote agglomeration, partially reversing the morphological benefits [29,30]. The identification of this crossover point is a practically significant finding that provides clear quantitative guidance for the optimisation of Ni–WO_3 synthesis.

CONCLUSION

A systematic study of hydrothermally synthesised Ni–WO_3 nanoparticles at doping concentrations of 2.5%, 5%, 7%, and 10% has established the following key findings. XRD confirmed the retention of the monoclinic gamma-WO_3 phase across all compositions with no secondary phases, progressive lattice expansion, and crystallite size reduction from 35 nm (undoped) to 22 nm (7% Ni), with microstrain increasing monotonically from 0.08% to 0.27%. FE-SEM revealed a systematic transition from compact quasi-spherical particles to an open, porous nanoparticulate architecture at 7% Ni, with inter-particle pores of 10–50 nm favourable for electrolyte access. EDAX confirmed successful Ni incorporation at concentrations closely matching nominal values, with slight oxygen sub-stoichiometry consistent with charge-compensating vacancy formation. FTIR demonstrated dopant-induced broadening and red-shift of the W=O and W–O–W vibrational modes, with an emerging Ni–O feature above 5% doping. UV–Visible spectroscopy revealed progressive optical band gap narrowing from 2.65 eV (undoped) to 2.35 eV (7% Ni). Cyclic voltammetry showed that 7% Ni–WO_3 delivered the highest specific capacitance and best rate capability, rationalised by the concurrent optimisation of grain boundary density, morphological porosity, and electronic conductivity at this doping level. These results establish 7% Ni–WO_3 as an optimised pseudocapacitive electrode material and provide a validated structure–property framework directly applicable to the rational design and optimisation of transition metal-doped WO_3 systems for electrochemical energy storage.

REFERENCES

1. Zheng, H., Ou, J. Z., Strano, M. S., Kaner, R. B., Mitchell, A., & Kalantar-zadeh, K. (2011). Nanostructured tungsten oxide: Properties, synthesis, and applications. Advanced Functional Materials, 21(12), 2175–2196.
2. Huang, Z.-F., Song, J., Pan, L., Zhang, X., Wang, L., & Zou, J.-J. (2015). Tungsten oxides for photocatalysis, electrochemistry, and phototherapy. Advanced Materials, 27(36), 5309–5327.
3. Shannon, R. D. (1976). Revised effective ionic radii and systematic studies of interatomic distances in halides and chalcogenides. Acta Crystallographica Section A, 32(5), 751–767.
4. Scherrer, P. (1918). Bestimmung der Größe und der inneren Struktur von Kolloidteilchen mittels Röntgenstrahlen. Nachrichten von der Gesellschaft der Wissenschaften zu Göttingen, 1918, 98–100.
5. Williamson, G. K., & Hall, W. H. (1953). X-ray line broadening from filed aluminium and wolfram. Acta Metallurgica, 1(1), 22–31.
6. Wang, G., Zhang, L., & Zhang, J. (2012). A review of electrode materials for electrochemical supercapacitors. Chemical Society Reviews, 41(2), 797–828.
7. Greenwood, N. N., & Earnshaw, A. (1997). Chemistry of the Elements (2nd ed.). Butterworth-Heinemann.
8. Deb, S. K. (1973). Optical and photoelectric properties and colour centres in thin films of tungsten oxide. Philosophical Magazine, 27(4), 801–822.

9. Bak, T., Nowotny, J., Rekas, M., & Sorrell, C. C. (2003). Defect chemistry and semiconducting properties of titanium dioxide: I. Intrinsic electronic equilibria. Journal of Physics and Chemistry of Solids, 64(7), 1043–1056.
10. Shen, L., Wang, J., Xu, G., Li, H., Dou, H., & Zhang, X. (2015). $NiCo_2S_4$ nanosheets grown on nitrogen-doped carbon foams as an advanced electrode for supercapacitors. Advanced Energy Materials, 5(3), 1400977.
11. Goldstein, J. I., Newbury, D. E., Michael, J. R., Ritchie, N. W. M., Scott, J. H. J., & Joy, D. C. (2018). Scanning Electron Microscopy and X-ray Microanalysis (4th ed.). Springer.
12. Yao, D. D., Rani, R. A., O'Mullane, A. P., Kalantar-zadeh, K., & Ou, J. Z. (2014). High performance electrochromic devices based on anodized nanoporous Nb_2O_5. Journal of Physical Chemistry C, 118(18), 10867–10873.
13. Bamwenda, G. R., & Arakawa, H. (2001). The visible light induced photocatalytic activity of tungsten trioxide powders. Applied Catalysis A: General, 210(1–2), 181–191.
14. Gao, W., Singh, N., Song, L., Liu, Z., Reddy, A. L. M., Ci, L., Vajtai, R., Zhang, Q., Wei, B., & Ajayan, P. M. (2011). Direct laser writing of micro-supercapacitors on hydrated graphite oxide films. Nature Nanotechnology, 6(8), 496–500.
15. Scanlon, D. O., Watson, G. W., Payne, D. J., Atkinson, G. R., Egdell, R. G., & Law, D. S. L. (2010). Theoretical and experimental study of the electronic structures of MoO_3 and MoO_2. Journal of Physical Chemistry C, 114(10), 4636–4645.
16. Conway, B. E. (1999). Electrochemical Supercapacitors: Scientific Fundamentals and Technological Applications. Kluwer Academic/Plenum.
17. Brezesinski, K., Wang, J., Haetge, J., Reitz, C., Steinmueller, S. O., Tolbert, S. H., Smarsly, B. M., Dunn, B., & Brezesinski, T. (2010). Pseudocapacitive contributions to charge storage in highly ordered mesoporous group V transition metal oxides. Journal of the American Chemical Society, 132(20), 6982–6990.
18. Simon, P., Gogotsi, Y., & Dunn, B. (2014). Where do batteries end and supercapacitors begin? Science, 343(6176), 1210–1211.
19. Augustyn, V., Simon, P., & Dunn, B. (2014). Pseudocapacitive oxide materials for high-rate electrochemical energy storage. Energy & Environmental Science, 7(5), 1597–1614.
20. Kotz, R., & Carlen, M. (2000). Principles and applications of electrochemical capacitors. Electrochimica Acta, 45(15–16), 2483–2498.
21. Wei, W., Cui, X., Chen, W., & Ivey, D. G. (2011). Manganese oxide-based materials as electrochemical supercapacitor electrodes. Chemical Society Reviews, 40(3), 1697–1721.
22. Jayalakshmi, M., & Balasubramanian, K. (2008). Simple capacitors to supercapacitors: An overview. International Journal of Electrochemical Science, 3(11), 1196–1217.
23. Brousse, T., Belanger, D., & Long, J. W. (2015). To be or not to be pseudocapacitive? Journal of the Electrochemical Society, 162(5), A5185–A5189.
24. Dubal, D. P., Ayyad, O., Ruiz, V., & Gomez-Romero, P. (2015). Hybrid energy storage: The merging of battery and supercapacitor chemistries. Chemical Society Reviews, 44(7), 1777–1790.
25. Simon, P., & Gogotsi, Y. (2008). Materials for electrochemical capacitors. Nature Materials, 7(11), 845–854.
26. Augustyn, V., Come, J., Lowe, M. A., Kim, J. W., Taberna, P.-L., Tolbert, S. H., Abruna, H. D., Simon, P., & Dunn, B. (2013). High-rate electrochemical energy storage through Li^+ intercalation pseudocapacitance. Nature Materials, 12(6), 518–522.
27. Miller, J. R., & Simon, P. (2008). Electrochemical capacitors for energy management. Science, 321(5889), 651–652.
28. Zhang, L. L., & Zhao, X. S. (2009). Carbon-based materials as supercapacitor electrodes. Chemical Society Reviews, 38(9), 2520–2531.
29. Burke, A. (2000). Ultracapacitors: Why, how, and where is the technology. Journal of Power Sources, 91(1), 37–50.
30. Arico, A. S., Bruce, P., Scrosati, B., Tarascon, J.-M., & van Schalkwijk, W. (2005). Nanostructured materials for advanced energy conversion and storage devices. Nature Materials, 4(5), 366–377.
31. Zhu, J., Tang, S., Xie, H., Dai, Y., & Meng, X. (2014). Hierarchically porous MnO_2 microspheres doped with homogeneously distributed Fe_3O_4 nanoparticles for

supercapacitors. ACS Applied Materials & Interfaces, 6(20), 17637–17646.

32. Stoller, M. D., Park, S., Zhu, Y., An, J., & Ruoff, R. S. (2008). Graphene-based ultracapacitors. Nano Letters, 8(10), 3498–3502.
33. Lokhande, C. D., Dubal, D. P., & Joo, O.-S. (2011). Metal oxide thin film based supercapacitors. Current Applied Physics, 11(3), 255–270.
34. Gao, T., Fjeld, H., Fjellvag, H., Norby, T., & Norby, P. (2009). In situ studies of structural stability and proton conductivity of beta-MoO_3. Energy & Environmental Science, 2(4), 386–394.
35. Porto, S. P. S., Fleury, P. A., & Damen, T. C. (1967). Raman spectra of TiO_2, MgF_2, ZnF_2, FeF_2, and MnF_2. Physical Review, 154(2), 522–526.

HOW TO CITE: Nakul Arun Barwat[1]*, G. N. Chaudhari[2], Structural, Morphological, Optical, And Electrochemical Properties Of Nickel-Doped Tungsten Trioxide (Ni–WO_3) Nanomaterials Synthesised By Hydrothermal Method For Supercapacitor Electrode Applications, Int. J. Sci. R. Tech., 2026, 3 (6), 855-867. https://doi.org/10.5281/zenodo.20685330